Gauge Conditions for Long-Term Numerical Black Hole Evolution With or Without Excision

Miguel Alcubierre[1], Bernd Brügmann[1], Denis Pollney[1],
Edward Seidel[1,2], and Ryoji Takahashi[1]

[1] Max-Planck-Institut für Gravitationsphysik, Albert-Einstein-Institut,
Am Mühlenberg 1, 14476 Golm, Germany
[2] National Center for Supercomputing Applications, Beckman Institute,
405 N. Mathews Ave., Urbana, IL 61801

Abstract. We extend previous work on 3D black hole excision to the case of distorted black holes, with a variety of dynamic gauge conditions that are able to respond naturally to the spacetime dynamics. We show that the combination of excision and gauge conditions we use is able to drive highly distorted, rotating black holes to an almost static state at late times, with well behaved metric functions, without the need for any special initial conditions or analytically prescribed gauge functions. Further, we show for the first time that one can extract accurate waveforms from these simulations, with the full machinery of excision or *no excision* and dynamic gauge conditions. The evolutions can be carried out for long times, far exceeding the longevity and accuracy of even better resolved 2D codes. While traditional 2D codes show errors in quantities such as apparent horizon mass of over 100% by $t \approx 100M$, and crash by $t \approx 150M$, with our new techniques the same systems can be evolved for more than hundreds of M's in full 3D with errors of only a few percent.

1 Introduction

The long term numerical evolution of black hole systems is one of the most challenging and important problems in numerical relativity. For black holes, the difficulties of accuracy and stability in solving Einstein's equations numerically are exacerbated by the special problems posed by spacetimes containing singularities. At a singularity, geometric quantities become infinite and cannot be handled easily by a computer.

Traditionally, in the 3+1 approach the freedom in choosing the slicing is used to slow down the approach of the time slices towards the singularity ("singularity avoidance"), while allowing them to proceed outside the black hole. Singularity avoiding slicings are able to provide accurate evolutions, allowing one to study black hole collisions and extract waveforms [1], but only for limited cases and evolution times. Combining short full numerical evolutions with perturbation methods, one can even study the plunge from the last stable orbit of two black holes [2]. But a dramatic breakthrough is required to push numerical simulations far enough to study orbiting black holes, requiring accurate evolutions exceeding time scales of $t \approx 100M$. In 3D, traditional approaches have not been able to reach such time scales, even in the case of Schwarzschild black holes.

A more promising approach involves cutting away the singularity from the calculation ("singularity excision"), assuming it is hidden inside an apparent horizon (AH) [3,4]. Although this work has been progressing, from early spherical proof of principle in [4] to recent 3D developments [5–8], beyond a few spherical test cases [9,10] it has yet to be used in conjunction with appropriate live gauge conditions designed to respond to both the dynamics of the black hole and the coordinate motion through the spacetime.

In this paper we extend recent excision work [7] to the case of distorted, dynamic black holes in 3D, using a new class of gauge conditions. These gauge conditions, which not only respond naturally to the true spacetime dynamics, but also *drive the system towards an almost static state at late times*, allow us to handle black holes without considering special initial coordinate systems, such as the Kerr-Schild type, which may be difficult or impossible to find during a generic black hole evolution. We show that not only are the evolutions accurate as indicated by the mass associated with the apparent horizon, but also that very accurate waveforms can be extracted with excision or *without* excision, even when the waves carry only a tiny fraction of the energy of the spacetime. We also show that the 3D evolutions of dynamic black holes we are now able to perform, are superior, in terms of accuracy, stability, and longevity, to previous dynamic 3+1 black hole simulations, whether they were carried out in full 3D or even when restricted to 2D. These results indicate that black hole evolution with new gauge conditions can be made to work under rather general circumstances, and can dramatically improve both the length of the evolutions, and the accuracy of the waveforms extracted, which will be crucial for gravitational wave astronomy.

2 Initial Data

For this paper we consider a series of single distorted black hole spacetimes [11,12] that have been used to model the late stages of black hole coalescence [13,14]. Following [11,12], the initial three-metric γ_{ab} is chosen to be

$$\mathrm{d}s^2 = \psi^4 \left[\mathrm{e}^{2q} \left(\mathrm{d}\eta^2 + \mathrm{d}\theta^2 \right) + \sin^2\theta \, \mathrm{d}\phi^2 \right] \ , \tag{1}$$

where the "Brill wave" function q is a general function of the spatial coordinates, subject to certain regularity and fall off restrictions, that can be tailored to produce very distorted 3D black holes interacting with nonlinear waves. The radial coordinate η is logarithmic in the cartesian radius r. There are two classes of data sets used here corresponding to even- and odd-parity distortions. The even-parity data have vanishing extrinsic curvature, while the cases containing an odd-parity component have nontrivial extrinsic curvature K_{ij}. As shown in [15,16], these distorted black hole data sets can include rotation as well, corresponding to spinning, distorted black holes that mimic the early merger of two orbiting black holes. Hence they make an ideal test case for the development of our techniques. We leave the details of the construction of these black hole initial data sets to [15,16].

An important point that we wish to emphasize is that such data are *not* of the Kerr-Schild form with ingoing coordinates at the horizon. That particular form of black hole initial data sets has been recently advocated as providing a more natural treatment for black hole excision since the coordinate system is adapted to inward propagation of quantities at the horizon [17]. However, it is not obvious that the physically desired initial data can always be written in the Kerr-Schild form (or, for that matter, in any other particular form). Furthermore, during an evolution, even if similar such coordinates are somehow actively enforced, it is probably not possible to have such a coordinate system in place at all times, when a new black hole forms. Hence, we prefer to be able to handle black hole data in any coordinate system, and apply coordinate conditions that naturally drive the system into a static state as the black hole system settles down to Kerr, from any starting point.

3 Evolution and Excision Procedures

Our simulations have been performed using what we refer to as the "BSSN" version of the 3+1 evolution equations [18–21], which we have found to have superior stability properties when compared to standard formulations.

The standard variables in the 3+1 formulation of ADM (Arnowitt-Deser-Misner, see [22]) are the 3-metric γ_{ij} and its extrinsic curvature K_{ij}. The gauge is determined by the lapse function α and the shift vector β^i. We will only consider the vacuum case. The evolution equations are

$$(\partial_t - \mathcal{L}_\beta)\, \gamma_{ij} \;= -2\alpha K_{ij} \;, \tag{2}$$

$$(\partial_t - \mathcal{L}_\beta)\, K_{ij} = -D_i D_j \alpha + \alpha(R_{ij} + K K_{ij} - 2K_{ik}K^k{}_j) \;, \tag{3}$$

and the constraints are

$$\mathcal{H} \;\equiv R + K^2 - K_{ij}K^{ij} = 0 \;, \tag{4}$$

$$\mathcal{D}^i \equiv D_j(K^{ij} - \gamma^{ij}K) = 0 \;. \tag{5}$$

Here $\mathcal{L}_\beta$ is the Lie derivative with respect to the shift vector β^i, D_i is the covariant derivative associated with the 3-metric γ_{ij}, R_{ij} is the three-dimensional Ricci Tensor, R the Ricci scalar, and K is the trace of K_{ij}.

We will use the BSSN form of these equations (Baumgarte, Shapiro [19], and Shibata, Nakamura [18]). One introduces new variables based on a trace decomposition of the extrinsic curvature and a conformal rescaling of both the metric and the extrinsic curvature. The trace-free part A_{ij} of the extrinsic curvature is defined by

$$A_{ij} = K_{ij} - \frac{1}{3}\gamma_{ij}K \;. \tag{6}$$

Assuming that the metric γ_{ij} is obtained from a conformal metric $\tilde{\gamma}_{ij}$ by a conformal transformation,

$$\gamma_{ij} = \psi^4 \tilde{\gamma}_{ij} \;, \tag{7}$$

we can choose a conformal factor ψ such that the determinant of $\tilde{\gamma}_{ij}$ is 1:

$$\psi = \gamma^{1/12} , \tag{8}$$
$$\tilde{\gamma}_{ij} = \psi^{-4}\gamma_{ij} = \gamma^{-1/3}\gamma_{ij} , \tag{9}$$
$$\tilde{\gamma} = 1 , \tag{10}$$

where γ is the determinant of γ_{ij} and $\tilde{\gamma}$ is the determinant of $\tilde{\gamma}_{ij}$. Instead of γ_{ij} and K_{ij} we can therefore use the variables

$$\phi = \ln\psi = \frac{1}{12}\ln\gamma , \tag{11}$$
$$K = \gamma_{ij}K^{ij} , \tag{12}$$
$$\tilde{\gamma}_{ij} = \mathrm{e}^{-4\phi}\gamma_{ij} , \tag{13}$$
$$\tilde{A}_{ij} = \mathrm{e}^{-4\phi}A_{ij} , \tag{14}$$

where $\tilde{\gamma}_{ij}$ has determinant 1 and $\tilde{A}_{ij}$ has vanishing trace. Furthermore, we introduce the conformal connection functions

$$\tilde{\Gamma}^i = \tilde{\gamma}^{jk}\tilde{\Gamma}^i{}_{jk} = -\partial_j\tilde{\gamma}^{ij} , \tag{15}$$

where $\tilde{\Gamma}^i{}_{jk}$ is the Christoffel symbol of the conformal metric. The second equality holds if the determinant of the conformal 3-metric $\tilde{\gamma}$ is actually unity (which is true analytically but may not be numerically). We call ϕ, K, $\tilde{\gamma}_{ij}$, $\tilde{A}_{ij}$, and $\tilde{\Gamma}^i$ the BSSN variables.

In terms of the BSSN variables the evolution equation (2) becomes

$$(\partial_t - \mathcal{L}_\beta)\,\tilde{\gamma}_{ij} = -2\alpha\tilde{A}_{ij} , \tag{16}$$
$$(\partial_t - \mathcal{L}_\beta)\,\phi = -\frac{1}{6}\alpha K , \tag{17}$$

while (3) leads to

$$(\partial_t - \mathcal{L}_\beta)\,\tilde{A}_{ij} = \mathrm{e}^{-4\phi}[-D_iD_j\alpha + \alpha R_{ij}]^{TF} + \alpha(K\tilde{A}_{ij} - 2\tilde{A}_{ik}\tilde{A}^k{}_j) , \tag{18}$$
$$(\partial_t - \mathcal{L}_\beta)\,K = -D^iD_j\alpha + \alpha(\tilde{A}_{ij}\tilde{A}^{ij} + \frac{1}{3}K^2) , \tag{19}$$

where TF denotes the trace-free part of the expression in brackets. On the right-hand side of (19) we have used the Hamiltonian constraint (4) to eliminate the Ricci scalar,

$$R = K_{ij}K^{ij} - K^2 = \tilde{A}_{ij}\tilde{A}^{ij} - \frac{2}{3}K^2 . \tag{20}$$

An evolution equation for $\tilde{\Gamma}^i$ can be obtained from (15) and (16),

$$\partial_t\tilde{\Gamma}^i = -2(\alpha\partial_j\tilde{A}^{ij} + \tilde{A}^{ij}\partial_j\alpha) - \partial_j\mathcal{L}_\beta\tilde{\gamma}^{ij} . \tag{21}$$

In this equation we use the momentum constraint (5) to substitute for the divergence of $\tilde{A}^{ij}$,

$$\partial_j\tilde{A}^{ij} = -\tilde{\Gamma}^i{}_{jk}\tilde{A}^{jk} - 6\tilde{A}^{ij}\partial_j\phi + \frac{2}{3}\tilde{\gamma}^{ij}\partial_jK . \tag{22}$$

One subtlety in obtaining numerically stable evolutions with the BSSN variables is precisely the question of how the constraints are used in the evolution equations. Several choices are possible and have been studied, see [23].

Note that in the preceding equations we are computing Lie derivatives of tensor densities. If the weight of a tensor density T is w, that is if T is a tensor times $\gamma^{w/2}$, then

$$\mathcal{L}_\beta T = [\mathcal{L}_\beta T]^{w=0}_\partial + wT\partial_k\beta^k \ , \tag{23}$$

where the first term denotes the tensor formula for Lie derivatives with the derivative operator ∂ and the second is the additional contribution due to the density factor. The density weight of $\psi = \mathrm{e}^\phi$ is $1/6$, so the weight of $\tilde{\gamma}_{ij}$ and $\tilde{A}_{ij}$ is $-2/3$ and the weight of $\tilde{\gamma}^{ij}$ is $2/3$. To be explicit,

$$\mathcal{L}_\beta\phi \ = \beta^k\partial_k\phi + \frac{1}{6}\partial_k\beta^k \ , \tag{24}$$

$$\mathcal{L}_\beta\tilde{\gamma}_{ij} = \beta^k\partial_k\tilde{\gamma}_{ij} + \tilde{\gamma}_{ik}\partial_j\beta^k + \tilde{\gamma}_{jk}\partial_i\beta^k - \frac{2}{3}\tilde{\gamma}_{ij}\partial_k\beta^k \ , \tag{25}$$

$$\mathcal{L}_\beta\tilde{\gamma}^{ij} = \beta^k\partial_k\tilde{\gamma}^{ij} - \tilde{\gamma}^{ik}\partial_k\beta^j - \tilde{\gamma}^{jk}\partial_k\beta^i + \frac{2}{3}\tilde{\gamma}^{ij}\partial_k\beta^k \ . \tag{26}$$

The evolution equation (21) for $\tilde{\Gamma}^i$ therefore becomes

$$\begin{aligned}\partial_t\tilde{\Gamma}^i = {} & \tilde{\gamma}^{jk}\partial_j\partial_k\beta^i + \frac{1}{3}\tilde{\gamma}^{ij}\partial_j\partial_k\beta^k + \beta^j\partial_j\tilde{\Gamma}^i - \tilde{\Gamma}^j\partial_j\beta^i + \frac{2}{3}\tilde{\Gamma}^i\partial_j\beta^j \\ & -2\tilde{A}^{ij}\partial_j\alpha + 2\alpha(\tilde{\Gamma}^i{}_{jk}\tilde{A}^{jk} + 6\tilde{A}^{ij}\partial_j\phi - \frac{2}{3}\tilde{\gamma}^{ij}\partial_j K) \ .\end{aligned} \tag{27}$$

In the second line we see the formula for a vector density of weight $2/3$, but since $\tilde{\Gamma}^i$ is derived from the Christoffel symbols we obtain extra terms involving second derivatives of the shift (the first line in the equation above).

On the right-hand sides of the evolution equations for $\tilde{A}_{ij}$ and K, (18) and (19), there occur covariant derivatives of the lapse function, and the Ricci tensor of the non-conformal metric. Since

$$\Gamma^k{}_{ij} = \tilde{\Gamma}^k{}_{ij} + 2(\delta^k_i\partial_j\phi + \delta^k_j\partial_i\phi - \tilde{\gamma}_{ij}\tilde{\gamma}^{kl}\partial_l\phi) \ , \tag{28}$$

where $\tilde{\Gamma}^k{}_{ij}$ is the Christoffel symbol of the conformal metric, we have for example

$$D^iD_i\alpha = \mathrm{e}^{-4\phi}(\tilde{\gamma}^{ij}\partial_i\partial_j\alpha - \tilde{\Gamma}^k\partial_k\alpha + 2\tilde{\gamma}^{ij}\partial_i\phi\partial_j\alpha) \ . \tag{29}$$

The Ricci tensor can be separated in two parts,

$$R_{ij} = \tilde{R}_{ij} + R^\phi_{ij} \ , \tag{30}$$

where $\tilde{R}_{ij}$ is the Ricci tensor of the conformal metric and R^ϕ_{ij} denotes additional terms depending on ϕ:

$$\begin{aligned}R^\phi_{ij} = {} & -2\tilde{D}_i\tilde{D}_j\phi - 2\tilde{\gamma}_{ij}\tilde{D}^k\tilde{D}_k\phi \\ & +4\tilde{D}_i\phi\ \tilde{D}_j\phi - 4\tilde{\gamma}_{ij}\tilde{D}^k\phi\ \tilde{D}_k\phi \ ,\end{aligned} \tag{31}$$

where $\tilde{D}_i$ is the covariant derivative associated with the conformal metric. The conformal Ricci tensor can be written in terms of the conformal connection functions as

$$\tilde{R}_{ij} = -\frac{1}{2}\tilde{\gamma}^{lm}\partial_l\partial_m\tilde{\gamma}_{ij} + \tilde{\gamma}_{k(i}\partial_{j)}\tilde{\Gamma}^k + \tilde{\Gamma}^k\tilde{\Gamma}_{(ij)k} + \tilde{\gamma}^{lm}\left(2\tilde{\Gamma}^k{}_{l(i}\tilde{\Gamma}_{j)km} + \tilde{\Gamma}^k{}_{im}\tilde{\Gamma}_{klj}\right) . \quad (32)$$

A key observation here is that if one introduces the $\tilde{\Gamma}^i$ as independent variables, then the principal part of the right-hand side of (18) contains the wave operator $\tilde{\gamma}^{lm}\partial_l\partial_m\tilde{\gamma}_{ij}$ but no other second derivatives of the conformal metric. This brings the evolution system one step closer to being hyperbolic.

One of the reasons why we have written out the BSSN system in such detail is to point out a subtlety that arises in the actual implementation if one wants to achieve numerical stability. In the computer code we do not use the numerically evolved $\tilde{\Gamma}^i$ in all places, but follow this rule:

- Partial derivatives $\partial_j\tilde{\Gamma}^i$ are computed as finite differences of the independent variables $\tilde{\Gamma}^i$ that are evolved using (27).
- In expressions that require $\tilde{\Gamma}^i$, not its derivative, we substitute $\tilde{\gamma}^{jk}\tilde{\Gamma}^i{}_{jk}(\tilde{\gamma})$, that is we do not use the independently evolved variable $\tilde{\Gamma}^i$ but recompute $\tilde{\Gamma}^i$ according to its definition (15) from the current values of $\tilde{\gamma}_{ij}$.

In practice we have found that the evolutions are far less stable if either $\tilde{\Gamma}^i$ is treated as an independent variable everywhere, or if $\tilde{\Gamma}^i$ is recomputed from $\tilde{\gamma}_{ij}$ before each time step. The rule just stated helps to maintain the constraint $\tilde{\Gamma}^i = -\partial_j\tilde{\gamma}^{ij}$ well behaved without removing the advantage of reformulating the principal part of the Ricci tensor.

In summary, we evolve the BSSN variables $\tilde{\gamma}_{ij}$, ϕ, $\tilde{A}_{ij}$, K, and $\tilde{\Gamma}^i$ according to (16), (17), (18), (19), and (27), respectively. The Ricci tensor is separated as shown in (30) with each part computed according to (31) and (32) respectively. The Hamiltonian and momentum constraints have been used to write the equations in a particular way. The evolved variables $\tilde{\Gamma}^i$ are only used when their partial derivatives are needed (the one term in the conformal Ricci tensor (32) and the advection term $\beta^k\partial_k\tilde{\Gamma}^i$ in the evolution equation for the $\tilde{\Gamma}^i$ themselves, (27)).

We use the simple excision approach described in [7]. Our excision algorithm is based on the following ideas: (a) Excise a *cube* contained inside the AH that is well adapted to cartesian coordinates; (b) Use a simple but stable boundary condition at the sides of the excised cube: copying of time derivatives from their values one grid point out along the normal directions; (c) Use standard centered (non-causal) differences in all terms except for advection terms on the shift (those that look like $\beta^i\partial_i$). For these terms we use second order upwind along the shift direction. These simplifications in excision reduce the complexity in the algorithm, avoid delicate interpolation issues near the excision boundary, and have allowed us to make rapid progress.

4 Numerics

The numerical time integration in our code uses an iterative Crank-Nicholson scheme with 3 iterations, see e.g. [23]. Derivatives are represented by second order finite differences on a Cartesian grid. We use standard centered difference stencils for all terms, except in the advection terms involving the shift vector (terms that look like $\beta^i \partial_i$). For these terms we use second order upwind along the shift direction. We have found the use of an upwind scheme in such advection-type terms crucial for the stability of our code. Notice that this is the only place in our implementation where any information about causality is used (i.e. the direction of the tilt in the light cones).

At the outer boundary we use a radiation (Sommerfeld) boundary condition. We start from the assumption that near the boundary all fields behave as spherical waves, namely we impose the condition

$$f = f_0 + \frac{u(r - vt)}{r} \; . \tag{33}$$

Where f_0 is the asymptotic value of a given dynamical variable (typically 1 for the lapse and diagonal metric components, and zero for everything else), and v is some wave speed. If our boundary is sufficiently far away one can safely assume that the speed of light is 1, so $v = 1$ for most fields. However, the gauge variables can easily propagate with a different speed implying a different value of v (see below where we discuss the gauge conditions).

In practice, we do not use the boundary condition (33) as it stands, but rather we use it in differential form:

$$\partial_t f + v \partial_r f - v \, \frac{(f - f_0)}{r} = 0 \; . \tag{34}$$

Since our code is written in Cartesian coordinates, we transform the last condition to

$$\frac{x_i}{r} \, \partial_t f + v \partial_i f + \frac{v x_i}{r^2} \, (f - f_0) = 0 \; . \tag{35}$$

We finite difference this condition consistently to second order in both space and time and apply it to all dynamic variables (with possible different values of f_0 and v) at all boundaries.

There is a final subtlety in our boundary treatment. Wave propagation is not the only reason why fields evolve near a boundary. Simple infall of the coordinate observers will cause some small evolution as well, and such evolution is poorly modeled by a propagating wave. This is particularly important at early times, when the above boundary condition introduces a bad transient effect. In order to minimize the error at our boundaries introduced by such non-wavelike evolution, we allow for boundary behavior of the form:

$$f = f_0 + \frac{u(r - vt)}{r} + \frac{h(t)}{r^n} \; , \tag{36}$$

with h a function of t alone and n some unknown power. This leads to the differential equation

$$\partial_t f + v\partial_r f - \frac{v}{r}\,(f - f_0) = \frac{vh(t)}{r^{n+1}}\,(1 - nv) + \frac{h'(t)}{r^n} \simeq \frac{h'(t)}{r^n} \quad \text{for large } r\ , \tag{37}$$

or in Cartesian coordinates

$$\frac{x_i}{r}\,\partial_t f + v\partial_i f + \frac{vx_i}{r^2}\,(f - f_0) \simeq \frac{x_i h'(t)}{r^{n+1}}\ . \tag{38}$$

This expression still contains the unknown function $h'(t)$. Having chosen a value of n, one can evaluate the above expression one point away from the boundary to solve for $h'(t)$, and then use this value at the boundary itself. Empirically, we have found that taking $n = 3$ almost completely eliminates the bad transient caused by the radiative boundary condition on its own.

5 Gauge Conditions

We will consider families of gauge conditions that can be used in principle with any 3+1 form of the Einstein's equations that allows a general gauge. However, the specific family we test in this paper is best motivated by considering the BSSN system introduced above. For the present purposes, of special importance are the following two properties of this formulation:

- The trace of the extrinsic curvature K is treated as an independent variable. For a long time it has been known that the evolution of K is directly related to the choice of a lapse function α. Thus, having K as an independent field allows one to impose slicing conditions in a much cleaner way.
- The appearance of the "conformal connection functions" $\tilde{\Gamma}^i$ as independent quantities. As already noted by Baumgarte and Shapiro [19], the evolution equation for these quantities can be turned into an elliptic condition on the shift which is related to the minimal distortion condition. More generally, one can relate the shift choice to the evolution of these quantities, again allowing for a clean treatment of the shift condition.

Our aim is to look for gauge conditions that at late times, once the physical system under consideration has settled to a final stationary state, will be able to drive the coordinate system to a frame where this stationarity is evident. In effect, we are looking for "symmetry seeking" coordinates of the type discussed by Gundlach and Garfinkle [24] that will be able to find the approximate Killing field that the system has at late times. In order to achieve this we believe that the natural approach is to relate the gauge choice to the evolution of certain combinations of dynamic quantities in such a way that the gauge will either freeze completely the evolution of those quantities (typically by solving some elliptic equations), or will attempt to do so with some time delay (by solving instead parabolic or hyperbolic equations).

We will consider the lapse and shift conditions in turn. Special cases of the gauge conditions that we will introduce here were recently used together with black hole excision with remarkable results in [7], but as we will show below, the gauge conditions are so powerful that in the cases tested, they work even without excision.

5.1 Slicing Conditions

The starting point for our slicing conditions is the "K-freezing" condition $\partial_t K =0$, which in the particular case when $K=0$ reduces to the well known "maximal slicing" condition. The K-freezing condition leads to the following elliptic equation for the lapse

$$\nabla^2 \alpha = \beta^i \partial_i K + \alpha K_{ij} K^{ij} \; , \tag{39}$$

with ∇^2 the Laplacian operator for the spatial metric γ_{ij}. In the BSSN formulation, once we have solved the elliptic equation for the lapse, the K-freezing condition can be imposed at the analytic level by simply not evolving K.

One can construct parabolic or hyperbolic slicing conditions by making either $\partial_t \alpha$ or $\partial_t^2 \alpha$ proportional to $\partial_t K$. We call such conditions "K-driver" conditions (see [25]). The hyperbolic K-driver condition has the form [7]

$$\partial_t^2 \alpha = -\alpha^2 f(\alpha)\, \partial_t K = \alpha^2 f(\alpha) \left[\nabla^2 \alpha - \beta^i \partial_i K - \alpha K_{ij} K^{ij} \right] \; , \tag{40}$$

where $f(\alpha)$ is an arbitrary positive function of α. From the above equation it is clear the lapse obeys a wave equation with a source term. The corresponding wave speed can be easily seen to be $v_\alpha = \alpha \sqrt{f(\alpha)}$, which explains the need for $f(\alpha)$ to be positive. Notice that, depending on the value of $f(\alpha)$, this wave speed can be larger or smaller than the physical speed of light. This represents no problem, as it only indicates the speed of propagation of the coordinate system, i.e. it is only a "gauge speed". The hyperbolic K-driver condition is closely related to the Bona-Massó family of slicing conditions [26]: $\partial_t \alpha = \alpha^2 f(\alpha) K$. Our new condition has the advantage of allowing for static solutions for which K itself is non-zero.

In our evolutions, we normally take $f = 2/\alpha$, since empirically we have found that such a choice has excellent singularity avoiding properties. Notice that inside a black hole, where the lapse typically collapses to very small values, this choice of f implies that the gauge speed v_α will be very large, much larger than the physical speed of light.

5.2 Shift Conditions

In the BSSN formulation, an elliptic shift condition is easily obtained by imposing the "Gamma-freezing" condition $\partial_t \tilde{\Gamma}^k =0$, or

$$\begin{aligned} &\tilde{\gamma}^{jk} \partial_j \partial_k \beta^i + \frac{1}{3} \tilde{\gamma}^{ij} \partial_j \partial_k \beta^k - \tilde{\Gamma}^j \partial_j \beta^i + \frac{2}{3} \tilde{\Gamma}^i \partial_j \beta^j + \beta^j \partial_j \tilde{\Gamma}^i \\ &-2 \tilde{A}^{ij} \partial_j \alpha - 2\alpha \left(\frac{2}{3} \tilde{\gamma}^{ij} \partial_j \mathrm{tr} K - 6 \tilde{A}^{ij} \partial_j \phi - \tilde{\Gamma}^i_{jk} \tilde{A}^{jk} \right) = 0 \; . \end{aligned} \tag{41}$$

Notice that, just as with the K-freezing condition for the lapse, once we have solved the previous elliptic equations for the shift, the Gamma-freezing condition can be enforced at an analytic level by simply not evolving the $\tilde{\Gamma}^k$.

The Gamma-freezing condition is closely related to the well known minimal distortion shift condition [27]. In order to see exactly how these two shift conditions are related, we write here the minimal distortion condition

$$\nabla_j \Sigma^{ij} = 0 \,, \tag{42}$$

where Σ_{ij} is the so-called "distortion tensor" defined as

$$\Sigma_{ij} := \frac{1}{2}\gamma^{1/3}\partial_t \tilde{\gamma}_{ij} \,, \tag{43}$$

with $\tilde{\gamma}_{ij}$ the same as before. A little algebra shows that the evolution equation for the conformal connection functions (27) can be written in terms of Σ_{ij} as

$$\partial_t \tilde{\Gamma}^i = 2\partial_j \left(\gamma^{1/3}\Sigma^{ij}\right) \,. \tag{44}$$

More explicitly, we have

$$\partial_t \tilde{\Gamma}^i = 2\mathrm{e}^{4\phi}\left[\nabla_j \Sigma^{ij} - \tilde{\Gamma}^i_{jk}\Sigma^{jk} - 6\Sigma^{ij}\partial_j \phi\right] \,. \tag{45}$$

We then see that the minimal distortion condition $\nabla^j \Sigma_{ij} = 0$, and the Gamma-freezing condition $\partial_t \tilde{\Gamma}^i = 0$ are equivalent up to terms involving first spatial derivatives of the spatial metric multiplied with the distortion tensor itself. In particular, all terms involving second derivatives of the shift are identical in both cases (but not so terms with first derivatives of the shift).

Just as it was the case with the lapse, we obtain parabolic and hyperbolic shift prescriptions by making either $\partial_t \beta^i$ or $\partial_t^2 \beta^i$ proportional to $\partial_t \tilde{\Gamma}^i$. We call such conditions "Gamma-driver" conditions. The parabolic Gamma driver condition has the form

$$\partial_t \beta^i = k_p \, \partial_t \tilde{\Gamma}^i \,, \qquad (k_p > 0) \,, \tag{46}$$

and the hyperbolic one

$$\partial_t^2 \beta^i = k_h \, \partial_t \tilde{\Gamma}^i - \eta \, \partial_t \beta^i \,, \qquad (k_h, \eta > 0) \,, \tag{47}$$

where k_p, k_h and η are positive functions of space and time. In the case of the hyperbolic Gamma-driver we have found it useful to add a dissipation term with coefficient η. Experience has shown that by tuning the value of this dissipation coefficient we can manage to almost freeze the evolution of the system at late times.

An important point that needs to be considered when using the hyperbolic Gamma-driver condition is that of the gauge speeds. Just as it happened with the lapse, the use of a hyperbolic equation for the shift introduces new "gauge speeds" associated with the propagation of the shift. In order to get an idea of

how these gauge speeds behave, we will consider for a moment the shift condition (47) for small perturbations of flat space (and taking η=0). From the form of $\partial_t \tilde{\Gamma}^i$ given by (27) we see that in such a limit the principal part of the evolution equation for the shift reduces to

$$\partial_t^2 \beta^i = k_h \left(\delta^{jk} \partial_j \partial_k \beta^i + \frac{1}{3} \delta^{ij} \partial_j \partial_k \beta^k \right) . \tag{48}$$

Consider now only derivatives in a given direction, say x. We find

$$\partial_t^2 \beta^i = k_h \left(\partial_x^2 \beta^i + \frac{1}{3} \delta^{ix} \partial_x \partial_x \beta^x \right) , \tag{49}$$

which implies

$$\partial_t^2 \beta^x = \frac{4}{3} k_h \partial_x^2 \beta^x , \tag{50}$$

$$\partial_t^2 \beta^q = k_h \partial_x^2 \beta^q \qquad q \neq x . \tag{51}$$

We can then see that in regions where spacetime is almost flat, the longitudinal part of the shift propagates with speed $v_{\rm long} = 2\sqrt{k_h/3}$ while the transverse part propagates with speed $v_{\rm trans} = \sqrt{k_h}$. In all the simulations presented below, we have chosen:

$$k_h = \frac{3}{4} \frac{\alpha^{n_1}}{\psi^{n_2}} , \tag{52}$$

with ψ the conformal factor coming from the initial data. The division by ψ^{n_2} (in this paper, all simulations are done by $n_1 = 0$ and $n_2 = 4$) helps to keep the shift small near the vicinity of the horizon. Since far from the black hole both α and ψ are close to 1, our choice implies that the longitudinal part of the shift will propagate with a speed of 1 (the speed of light), and the transverse part will propagate with a speed equal to $\sqrt{3}/2$. At the boundaries, we simply use the speed of light for all shift components. This will introduce an error for the transverse components, but in all our simulations those components are typically very small close to the boundaries.

6 Results

The first example we show is Schwarzschild, written in the standard isotropic coordinates used in many black hole evolutions. Note that with this initial data and our starting gauge conditions, the black hole should evolve rapidly. If α and β^i were held fixed at their initial values, the slice would hit the singularity at $t = \pi M$ and crash. Instead, α and β^i work together with the excision to rapidly drive the system towards a static state, without any special choice of initial conditions.

In Fig. 1 we show the radial metric function g_{rr}/ψ^4 vs. time. The grid covers an octant with 128^3 points ($\Delta x = 0.1M$, $M = 2$). Notice that the metric begins

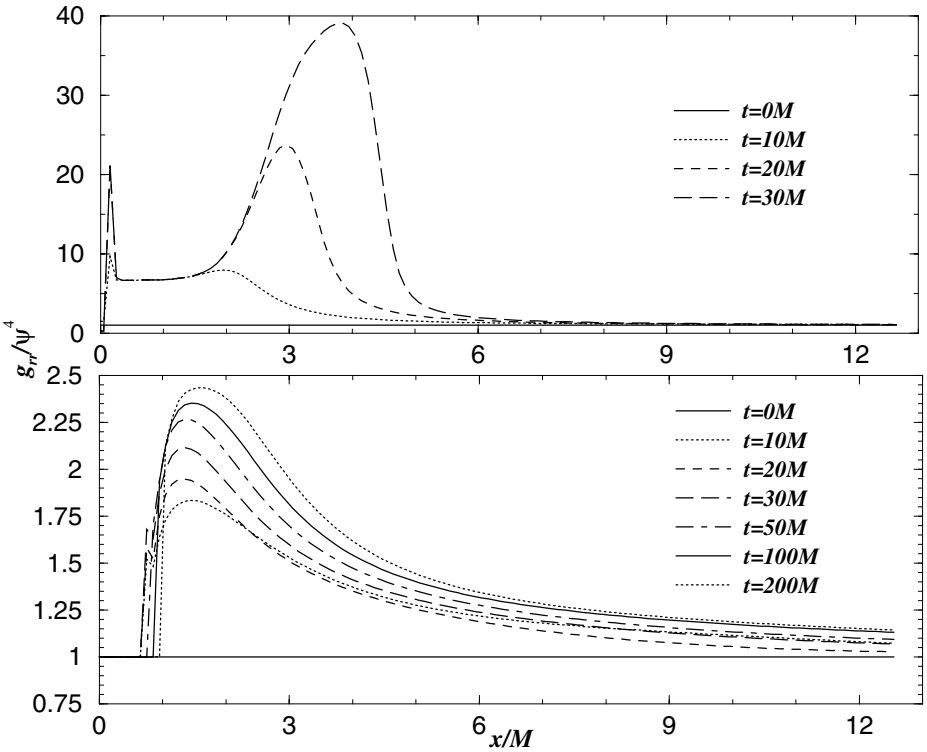

Fig. 1. We show the radial metric function g_{rr}/ψ^4 for a Schwarzschild black hole along the $x-$axis, constructed from the cartesian metric components, as it evolves with time. The upper panel shows the grid-stretching in the metric for singularity avoiding slicing with vanishing shift and no excision, while the lower panel shows the metric for the new gauge conditions with an excision box inside a sphere of radius $1M$. Note the difference in the vertical scales. Without shift and excision the metric grows out of control, while with shift and excision a peak begins to form initially as grid stretching starts, but later freezes in as the shift drives the black hole into a static configuration (note the time labels)

to grow, as it does without a shift, but as the shift builds up the growth slows down significantly. At this stage, the system is effectively static, even though we started in the highly dynamic isotropic coordinates. We also show the time development of α and β^r in Fig. 2, which evolve rapidly at first but then effectively freeze, bringing the system towards an almost static configuration by $t = 10M$. The evolution then proceeds only very slowly until the simulation is stopped well after $t = 200M$.

In Fig. 3 we show the AH mass $M_{\rm AH}$, determined with a 3D AH finder [28]. For comparison, we also show the value of $M_{\rm AH}$ obtained from a highly resolved 2D simulation with zero shift and no excision, and for the 3D run without shift. While the 3D simulation with shift and excision continues well beyond $t = 200M$, the 2D result becomes very inaccurate and the code crashes due to axis

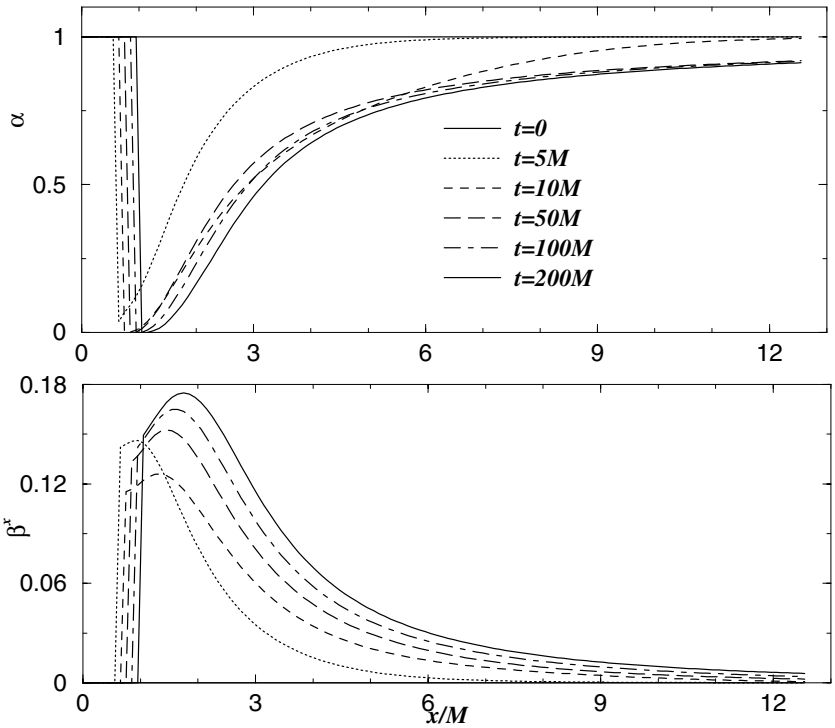

Fig. 2. We show the lapse and shift for the excision evolution of a Schwarzschild black hole. After around 10M, the lapse and shift freeze in as the system is driven to a static configuration. The size of the excision box was allowed to grow with the change in the coordinate location of the AH

instabilities by $t = 150M$, and the 3D run without shift crashes already by $t = 50M$. Notice that in the 2D case, after around $t = 35M$, $M_{\rm AH}$ grows rapidly due to numerical errors associated with grid stretching, and the AH finder ultimately fails as the code crashes. With excision and our new gauge conditions, the 3D run has less than a few percent error by $t = 200M$, while the 2D case has more than 100% error before it crashes at $t \approx 150M$. For the excision run, notice also that while there is some initial evolution in the metric and the coordinate size of the AH (see Figs. 1 and 2) the AH mass changes only very little. With new gauge conditions, we also find out that the 3D run without excision produces same results as with excision!

Next, we turn to a truly dynamic, even-parity distorted black hole. This system contains a strong gravitational wave that distorts the black hole, causing it to evolve, first nonlinearly, and then oscillating at its quasi-normal frequency, finally settling down to a static Schwarzschild black hole. This provides a test case for our techniques with dynamic, evolving black hole spacetimes, and allows us to test our ability to extract gravitational waves with excision for the first time. In this case, in the language of [15], we choose the Brill wave parameters

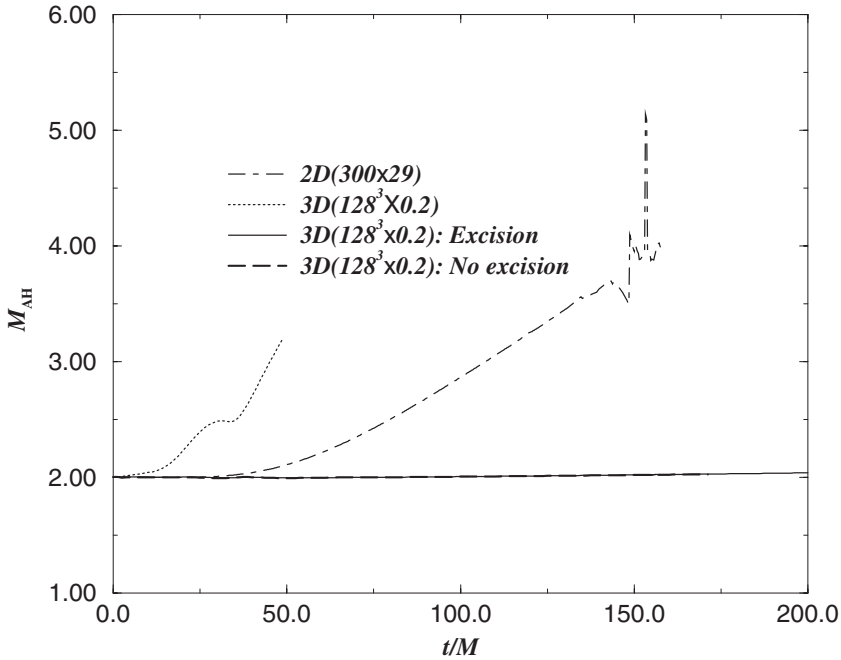

Fig. 3. The solid and long dashed lines show the development of the AH mass $M_{\rm AH}$, determined through a 3D AH finder, for the excision and no *no* excision simulation of a Schwarzschild black hole shown above, while the dot-dashed and dot lines show the AH mass obtained using 2D and 3D codes with zero shift and no excision. The 2D code crashes at around $t = 150M$, the 3D run without shift crashes around $t = 50M$, while the 3D runs with shift and excision (or) *no* excision reach an effectively static state and the error remains less than a few percent even after $t = 200M$

to be $Q_0 = 0.5$, $\eta_0 = 0$, $\sigma = 1$, corresponding to a highly distorted black hole with $M = 1.83$.

In Fig. 4 we show the AH mass $M_{\rm AH}$ as a function of time for the distorted black hole simulations carried out in both 2D and 3D. $M_{\rm AH}$ grows initially as a nonlinear burst of gravitational waves is absorbed by the black hole, distorting it strongly, but then levels off as the black hole goes into a ring-down phase towards Schwarzschild.

In the 3D cases, the dynamic gauge conditions and excision or *no* excision quickly drive the evolution towards an almost static configuration, as the system itself evolves towards a static Schwarzschild black hole. The evolution is continued until terminated at around $t = 300M$. Even in this highly dynamic system, no specialized form of initial data or lapse and shift are needed; our gauge choices naturally drive the system to a static state as desired. To our knowledge, distorted black holes of this type have never been evolved for so long, nor with such accuracy, in either 2D or 3D. By comparison, in the more highly resolved 2D case with zero shift and no excision, the familiar grid stretching effects allowed by the

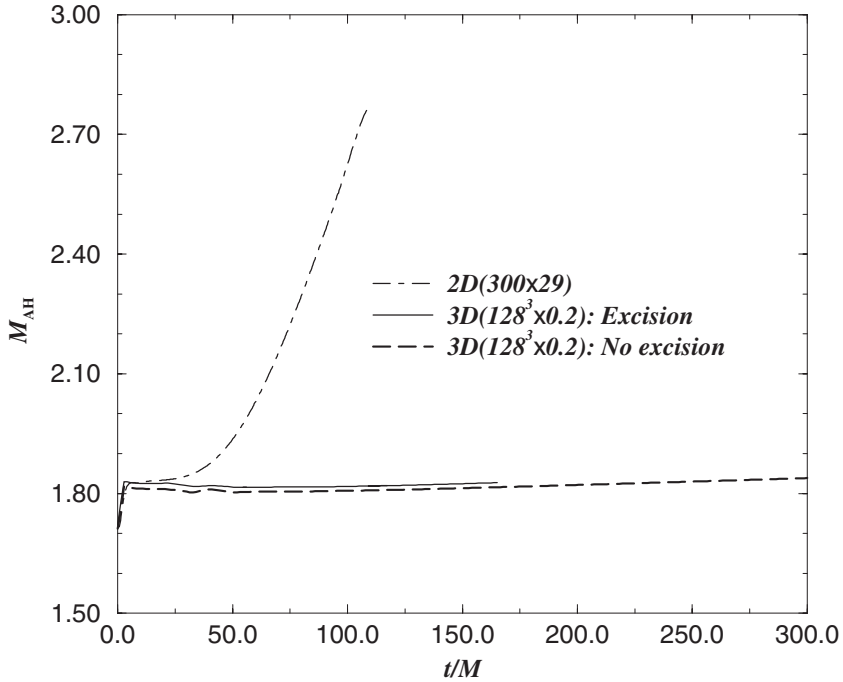

Fig. 4. We show the AH masses $M_{\rm AH}$ for a black hole with even-parity distortion for the 2D (no excision, no shift) and 3D (excision and *no* excision, shift) cases. The 3D result continues well past $300M$, while the 2D result becomes very inaccurate and crashes by $t = 100M$

gauge choice lead to highly inaccurate evolutions after some time with the error in $M_{\rm AH}$ again approaching 100% when the code finally crashes at $t \approx 100M$.

In Fig. 5, we show the results of extracting waves from the evolution of this highly distorted black hole. Using the standard gauge-invariant waveform extraction technique, the Zerilli function is shown for both the 2D and 3D simulations discussed above. There is a slight but physically irrelevant phase difference in the two results due to differences in the slicing; otherwise the results are remarkably similar.

This shows conclusively that the excision or *no* excision and live gauge conditions do not adversely affect the waveforms, even if they carry a small amount of energy (around $10^{-3}M_{\rm ADM}$ in this case).

We now turn to a rather different type of distorted black hole, including rotation and general even- and odd-parity distortions. In the language of [15,16], the parameters for this simulation are $Q_0 = 0.5$, $\eta_0 = 0$, $\sigma = 1$, $J = 35$, corresponding to a rotating distorted black hole with $M = 7.54$ and an effective rotation parameter $J/M^2 = 0.62$. Previously, such data sets could be evolved only to about $40M$ [14]. Again, for the purposes of this paper we have chosen an axisymmetric case so that we can compare the results to those obtained with a 2D code. Since this example is much more demanding, we have found it im-

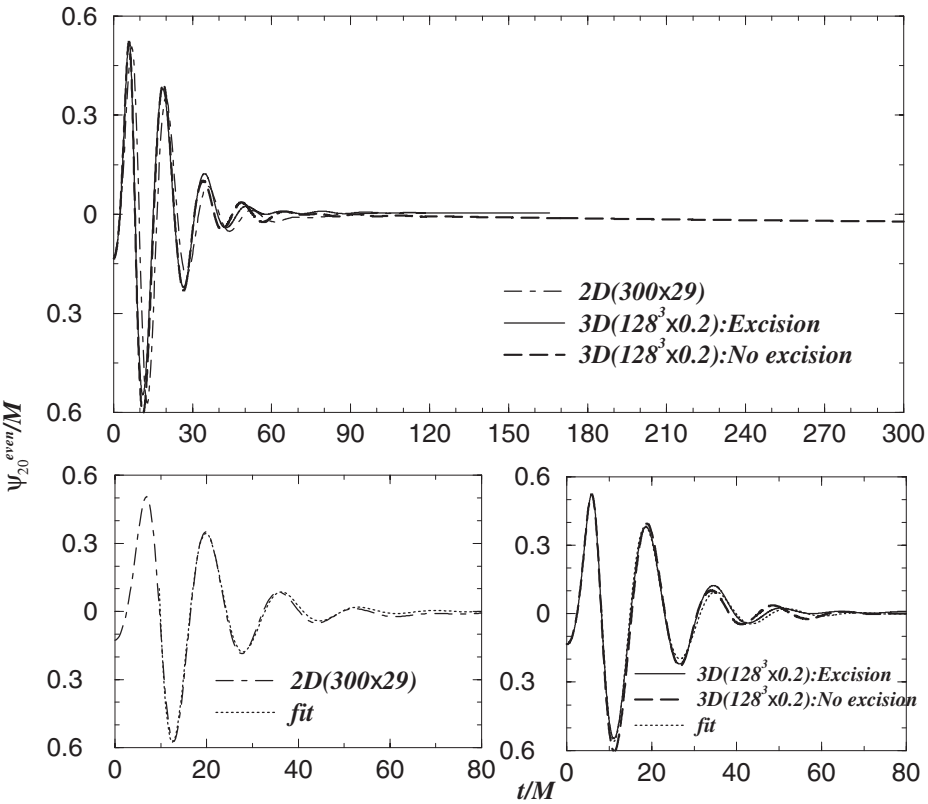

Fig. 5. The solid and long dashed lines show the result of the $\ell = 2, m = 0$ waveform extraction at a radius $5.45M$ for the even-parity distorted black hole described on the text, while the dashed line shows the result of the same simulation carried out in the 2D code. We also show a fit to the two lowest QNM's of the black hole for 2D and 3D separately, using numerical data from $t = 9M$ to $t = 80M$

portant in order to increase the accuracy of our runs to perform a single initial maximal solve to reduce the initial gauge dynamics. The gauge conditions used work well even in the presence of rotation: the shift drives the system towards a static *Kerr* black hole spacetime after the true dynamics settle down. The metric functions (not shown) evolve in a similar way to those shown before, essentially freezing at late times.

In Fig. 6, we show the extracted waveforms, now computed using the imaginary part of the Newman-Penrose quantity Ψ_4 (e.g. [2]), which includes contributions from all $\ell-$modes at the same time. The results from the 2D and 3D codes agree very closely, except for a slight phase shift due to slicing differences, until the 2D code becomes inaccurate and later crashes. The 3D simulation continues well beyond this point, and is terminated at $t = 140M$.

Figure 7 shows the snapshots of the apparent horizon with shift vectors for rotating 3D distorted. T shows the coordinate time so that the last picture

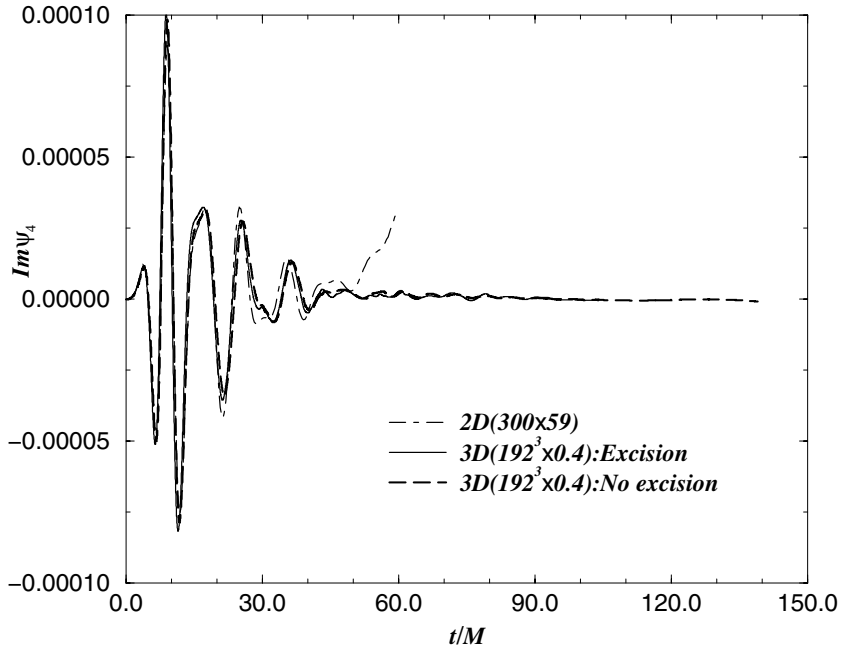

Fig. 6. The solid and long dashed lines show the a imaginary part of ψ_4 at a radius $3.94M$ and $\theta = \phi = \pi/4$ for rotating 3D distorted black hole, while the dot-dash line shows the same initial date by the 2D code which crashes around $60M$

shows them at around $t = 40M$. As the shift drives the system towards a static Kerr black hole spacetime, horizon grows until certain time and then oscillates towards a static Kerr black hole.

7 Conclusions

We have extended recently developed 3D black hole excision techniques, using a new class of live gauge conditions that *dynamically drive* the black hole system towards an essentially static state at late times, when the system itself settles to a stationary Kerr black hole. Our techniques have been tested on highly distorted, rotating black holes, are shown to be very robust, and require no special coordinate systems or special forms of initial data. For the first time, excision is tested with wave extraction, and waveforms are presented and verified. The results are shown to be more accurate, and much longer lived, than previous 3D simulations and even better resolved 2D simulations of the same initial data. Such improvements in black hole excision are badly needed for more astrophysically realistic black hole collision simulations, which are in progress and will be reported elsewhere.

Furthermore, we have found that the new gauge conditions can bring the evolution to an almost static state even *without* excision. Although we could

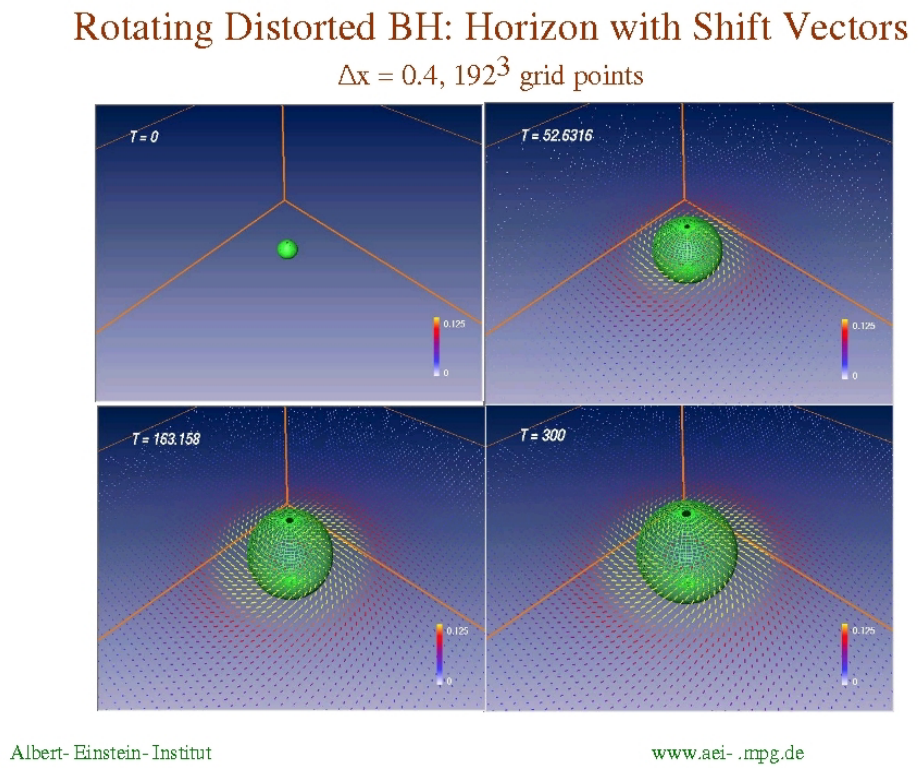

Fig. 7. We show snapshots of the apparent horizon with shift vectors for rotating 3D distorted black hole. T shows the coordinate time so that the last picture shows them at around $t = 40M$

show some primitive results, we are currently investigating properties of new gauge conditions [29]. We will also report these results in further publications.

Acknowledgements

Calculations were performed using the Cactus code at AEI, NCSA, PSC, and RZG.

References

1. M. Alcubierre *et al.*: Phys. Rev. Lett. **87**, 271103 (2001)
2. J. Baker *et al.*: Phys. Rev. Lett. **87**, 121103 (2001)
3. J. Thornburg: Class. Quantum Grav. **4**, 1119 (1987)
4. E. Seidel, W.-M. Suen: Phys. Rev. Lett. **69**, 1845 (1992)
5. G. B. Cook *et al.*: Phys. Rev. Lett **80**, 2512 (1998)
6. R. Gomez *et al.*: Phys. Rev. Lett. **80**, 3915 (1998)
7. M. Alcubierre, B. Brügmann: Phys. Rev. **D63**, 104006 (2001)

8. S. Brandt *et al.*: Phys. Rev. Lett. **85**, 5496 (2000)
9. P. Anninos *et al.*: Phys. Rev. **D52**, 2059 (1995)
10. G. E. Daues: Ph. D. Thesis, Washington University, St. Louis, Missouri (1996)
11. S. Brandt, E. Seidel: Phys. Rev. **D54**, 1403 (1996)
12. S. Brandt, E. Seidel: Phys. Rev. **D52**, 856 (1995)
13. K. Camarda, E. Seidel, Phys. Rev. **D59**, 064019 (1999)
14. J. Baker *et al.*: Phys. Rev. **D62**, 127701 (2000)
15. S. Brandt, K. Camarda, E. Seidel: In *Proceedings of the 8th Marcel Grossmann Meeting on General Relativity*, ed. by T. Piran (World Scientific, Singapore, 1999) pp. 741–743
16. S. Brandt, K. Camarda, E. Seidel, R. Takahashi: in preparation (unpublished)
17. R. A. Matzner, M. F. Huq, D. Shoemaker: Phys. Rev. **D59**, 024015 (1999)
18. M. Shibata, T. Nakamura: Phys. Rev. **D52**, 5428 (1995)
19. T. W. Baumgarte, S. L. Shapiro: Physical Review **D59**, 024007 (1999)
20. M. Alcubierre *et al.*: Phys. Rev. **D61**, 041501 (R) (2000)
21. M. Alcubierre *et al.*: Phys. Rev. **D62**, 124011 (2000)
22. J. York: In *Sources of Gravitational Radiation*, ed. by L. Smarr (Cambridge University Press, Cambridge, England, 1979)
23. M. Alcubierre *et al.*: Phys. Rev. **D62**, 044034 (2000)
24. D. Garfinkle, C. Gundlach: Class. Quantum Grav. **16**, 4111 (1999)
25. J. Balakrishna *et al.*: Class. Quantum Grav. **13**, L135 (1996)
26. A. Arbona, C. Bona, J. Massó, J. Stela: Phys. Rev. **D60**, 104014 (1999)
27. L. Smarr, J. York: Phys. Rev. **D17**, 2529 (1978)
28. M. Alcubierre *et al.*: Class. Quantum Grav. **17**, 2159 (2000)
29. M. Alcubierre *et al.*: in preparation (unpublished)